IEEE Access
Multidisciplinary ⋮ Rapid Review ⋮ Open Access Journal

Received June 13, 2021, accepted July 15, 2021, date of publication August 9, 2021, date of current version August 23, 2021.

Digital Object Identifier 10.1109/ACCESS.2021.3103580

Estimation of Chaotic Surface Pressure Characteristics of Ice Accreted Airfoils–A 0-1 Test Approach

S. NADARAJA PILLAI[1], AAKHASH SUNDARESAN[1], R. GOPAL[2], S. B. M. PRIYA[3], AMJAD ALI PASHA[4], ABDUL ZUBAR HAMEED[5], ABDUL GANI ABDUL JAMEEL[6,7], V. MAHENDRA REDDY[8], AND KHALID A. JUHANY[4]

[1]Turbulence and Flow Control Laboratory, School of Mechanical Engineering, SASTRA Deemed University, Thanjavur, Tamil Nadu 613401, India
[2]Centre for Nonlinear Science and Engineering, School of Electrical and Electronics Engineering, SASTRA Deemed University, Thanjavur, Tamil Nadu 613401, India
[3]School of Electrical and Electronics Engineering, SASTRA Deemed University, Thanjavur, Tamil Nadu 613401, India
[4]Aerospace Engineering Department, King Abdulaziz University, Jeddah 21589, Saudi Arabia
[5]Department of Industrial Engineering, Faculty of Engineering, King Abdulaziz University, Jeddah 21589, Saudi Arabia
[6]Department of Chemical Engineering, King Fahd University of Petroleum & Minerals, Dhahran 31261, Saudi Arabia
[7]Center for Refining & Advanced Chemicals, King Fahd University of Petroleum & Minerals, Dhahran 31261, Saudi Arabia
[8]Department of Mechanical Engineering, Indian Institute of Technology Kharagpur, Kharagpur, West Bengal 721302, India

Corresponding author: S. Nadaraja Pillai (nadarajapillai@mech.sastra.edu)

This work was supported by the Deanship of Scientific Research (DSR), King Abdulaziz University, Jeddah, under Grant DF-758-135-1441.

ABSTRACT Airfoils have their respective applications in almost every engineering field ranging from wind turbine blades, aircraft, and cooling fans to sophisticated electronic components. Thus, the flow over the airfoils is of primary focus to engineers in developing appropriate applications to meet the current standards in technology as well as demands. However, the underlying surface pressure characteristics need significant attention to understand the flow over airfoils completely. Generally, the flow over an airfoil and the time series pressure on the surface is linear and hence the aerodynamic forces are considered to be linear. But as the flow is perturbed due to external disturbances, nonlinearities creep in, and the surface pressure characteristics exhibit nonlinear behaviour. The ice accretion on the leading edge of the airfoil was witnessed to be an opportunity to investigate the nonlinear surface pressure characteristics. The current experimental study aims to investigate the dynamics of the surface pressure characteristics of four distinct ice geometries on the NACA0012 airfoil at a Reynolds number of 2×10^5. The angle of attack of the airfoil was varied from $0°$ to $24°$ with an increment of $3°$. The 0-1 test for chaos was applied to the ice accreted airfoils at all the pressure ports on the suction surface of the airfoil. The test gives a single value for K, known as the asymptotic growth rate of the mean squared displacement. The value of $K = 0$ implies that the underlying dynamics could be periodic and when the value of $K = 1$, the underlying dynamics show aperiodicity and hence chaos. The horn iced airfoil performed significantly weaker compared to other ice accretion geometries because a significantly higher amount of chaos was produced in the flow field due to the presence of a geometry resembling a separation bubble. This aided in the substantial increment in drag and loss of lift for the horn ice accreted airfoil.

INDEX TERMS Brownian motion, chaos, horn ice, ice accretion, rime ice, separation bubble, 0-1 test.

I. INTRODUCTION

Airfoils are the predominant pillars, which support aviation and wind turbine industries in delivering quality solutions and meeting public demands. They are omnipresent with their usage in wind turbine blades, rotor blades, aircraft, Unmanned Aerial Vehicles (UAV's), and much more. Hence, a thorough understanding of their underlying dynamics must be acknowledged and is deemed necessary to judge their aerodynamic performance. Several external factors that

The associate editor coordinating the review of this manuscript and approving it for publication was Ludovico Minati.

unfavorably modify the geometry of the airfoil could deteriorate the performance of the airfoil to a certain extent that is not appreciable. These factors could include accretion of ice on the leading edge of the blade profile, accumulation of dirt (foreign particles), etc. Harvesting wind energy in wide cold regions is popular due to the fact of the much denser air and available wind potential. It could be acknowledged that these wind turbines situated in the cold climatic regions are more prone to icing and have devastating effects on the performance and power production of wind turbines [1]. In the cold regions, the ice accretion on wind turbine blades is of great concern to both aerodynamicists and structural engineers as it causes the degradation of aerodynamic performance and power production. The formation of ice shape on the surface of the airfoil could depend mainly on the size of the Supercooled Large Droplet (SLD), impingement behaviour, atmospheric temperature and interaction with the solid boundary. The ice accretion is witnessed to be a key culprit in the decrement of aerodynamic performance. Due to the formation of peculiar ice shapes, the flow over the airfoil is aerodynamically disturbed, and the flow-field downstream of the airfoil could be chaotic and pave the way for large-amplitude fluctuations in pressure. This could induce additional stresses in the hazardous material.

The problem of icing on wind turbines was witnessed to be a major hindrance to the power production with a 20% to 50% decrease in the aerodynamic performance (Yirtici *et al.* 2016), leading to reductions of up to 17% in the Annual Energy Production (AEP). A few other problems caused by icing on wind turbines other than loss in power production; could include the disrupted blade aerodynamics, overloading due to delayed stall, elevated fatigue stresses and, imbalance caused due to ice loads and wind loading [3], in addition to the damage caused due to the shedding of ice chunks [4]. Also, it is observed that the ice thickness and the ice shape have a major impact on the unsteady aerodynamic coefficients [5] and occurs in the galloping phenomenon [6], [7]. It could also be prognosticated that the cut in and cut out speeds stand as limiting factors to the wind velocity profile of a wind turbine. Hence, this parameter could directly impact the range of operation of any wind turbine. Therefore, the present experimental study could aid the design engineers in providing appropriate measures to safeguard the operation, keeping in mind the physics of ice accretion and its influence on the surface pressure characteristics.

Predominantly, the need to investigate the flow over a modified airfoil surface has cultivated an interest in the minds of scientists and engineers; however, determination of the surface pressure characteristics in addition to the underlying dynamics is quite challenging thus, requiring a clear and concise understanding. Reference [3] studied the effects of ice accretion on both the symmetrical and unsymmetrical airfoils under different operating and geometric conditions, expressing the fact that the ice accretion contributes to the loss in the aerodynamic performance of the blade profile. Many researchers have claimed the leading edge to be the most susceptible part for the formation of ice [8]–[10] put forth the effect of atmospheric temperature and droplet size variation on the ice accretion of wind turbine blades. It was claimed that the atmospheric temperature and the droplet size were some of the key factors affecting the rate and shape of ice growth. The physical process that is involved during the atmospheric ice accretion is the collision of the supercooled liquid droplets on the surface of the wind turbine blades [11]. When the temperature of the atmosphere is such that the moisture in it exists in the liquid-solid interface, the supercooled liquid droplets acquire enough energy through collision and undergo a phase transformation from liquid to solid thereby, leading to the accretion of ice crystals on the surface of the blade profile. This modifies the original profile of the wind turbine blade and significantly affects the aerodynamic performance. Reference [12] put forth the effects of icing severity and wind turbine torque characteristics through various ice accretion tests [13] claimed that the outer part of the blade, usually at $r/R = 0.8$ (radial direction), contributed significantly to the blade aerodynamics. Also, this region of the blade was claimed to be affected during the icing process with a maximum of 40% power degradation. In [14] claimed that the rotor performance deteriorates significantly with an increase in the ice thickness on the blade. The ice accretion on the leading edge of the blade's airfoil section at $r/R = 0.95$ was witnessed to be highly correlated with the power loss among the tested icing cases.

In general, four major classes of ice accretion geometries involving the roughness ice, horn ice, streamwise ice, and spanwise – ridge ice were reported [8]. Also, it was claimed that the horn ice, when compared to the roughness and streamwise ice, contributed majorly to the decrement in the aerodynamic performance due to the formation of laminar separation bubbles on the suction surface of the airfoil. These separation bubbles were witnessed to dominate the flow field and contribute to the loss of lift coefficient and increment in the drag coefficient. Also, the overall pressure distribution around the airfoil was witnessed to be affected by a significant amount. Different researchers have made attempts towards studying the effects of ice formation on the airfoil [3], [9],. The approach to study the effect of ice accretion; predominantly included the artificial ice templates, Icing Research Tunnel, CFD simulations. These investigations involved the intervention of pure experimental, purely computational, or both experimental and numerical methods. The article [16] put forth the effects of water droplet Median Volume Diameter (MVD) on ice shapes and claimed that; as the MVD increases, the droplet size distribution becomes broader.

Generally, when the flow over an airfoil is smooth and periodic, it could be witnessed that the performance coefficients exhibit linear dynamics. When the flow over an airfoil remains attached along with the distance of the chord or becomes detached in a very short distance from the leading edge along the chord, it could imply a qualitative change

in the flow pattern [17]. The nonlinearities creep in when the flow around the airfoil transits from being periodic to chaotic. Hence, various studies have been carried out to understand the flow pattern and unsteady flow-fields around the airfoils. Generally, the flow around the airfoil gradually loses its periodic structure as the angle of attack of the airfoil increases [18]. This possibly could arise due to the fact when the flow cannot maintain its momentum against the adverse pressure gradient and hence, leading to the flow separation. The separated flow is usually an unsteady flow that traverses downstream of the airfoil and hence could lead to unsteady aerodynamic forces. The aperiodicity in the flow field could be captured using high precision techniques involving the Laser-Induced Fluorescence (LIF) technique and Particle Image Velocimetry [19]. It was acknowledged that these unsteady aerodynamic forces tend to exhibit nonlinear behaviour, possibly due to the inviscid effects and flow separation predominantly [17]. Considering the previous statement, the nonlinearities in the flow around an airfoil could arise from either the structural point of view or could be due to the flow itself being aperiodic. The aerodynamic flow nonlinearities could include gust, free stream turbulence, external excitations, ice accretion on the leading edge of the airfoil, etc. Hence, when the ice accretes on the surface of the airfoil, the flow around the airfoil becomes nonlinear, influencing the surface pressure characteristics and posing a challenge for the investigation of the aerodynamic parameters. There are many proposed classical techniques to distinguish the periodic and chaotic dynamics of a system which include Lyapunov exponent analysis, Lagrangian coherent structures, Recurrence Quantification Analysis (RQA), etc [17], [20], [21]. One such non-classical method is the evolution of the 0-1 test introduced by [22]. The 0-1 test for chaos is acknowledged to be less susceptible to noise, and hence, this eliminates the usage of standard pre-processing noise reduction techniques and is relatively computationally robust in distinguishing between regular and chaotic dynamics [22]–[24]. This test could be viewed as a method for distilling a binary quantity from the power spectrum and involves direct application on the time series data.

Although many attempts have been made in determining the surface pressure characteristics of the ice-accreted airfoil using standard procedures, the 0-1 test being applied to the ice-accreted airfoil to determine the underlying dynamics to ascertain the surface pressure characteristics is first of its kind. The authors in the present work evaluate the surface pressure characteristics of ice accreted airfoils with the aid of a novel approach known as the 0-1 test approach. The authors demonstrate the physics of flow separation and flow transition from laminar to a turbulent one through the computation of the asymptotic growth rate of the mean squared displacement of the translational variables, i.e., the 0-1 test innovatively distinguishes the surface pressure characteristics between periodic, chaotic, and transitory dynamics of an ice-accreted airfoil with a single value K = 0 or K = 1. This way, one can understand the flow field around the airfoil, which could aid in performance optimization and curb the hazards of icing on wind turbine blades. The ice templates were geometrically modeled from existing literature [16] and engineered to be used in the current experimental study.

The paper is organized as follows: An overview of the 0-1 test is put forth in section 2 to facilitate the readers with the mathematical background of the test and to provide insights as to why the test holds beneficial for the current research work. The organization of the experimental setup and methodologies are discussed in section 3. In section 4, the results of the 0-1 test, along with the aerodynamic parameters and its correlation with the standard time series plots, would be explained to gain significant insights into the surface pressure characteristics of an ice accreted airfoil.

II. UNDERSTANDING OF THE 0-1 TEST APPROACH

The 0-1 test for determining the periodic or chaotic dynamics of a deterministic dynamical system was developed by [22]. The speciality of the test, when compared to other methods of distinguishing periodic and chaotic dynamics, is that the nature of the dynamical system is irrelevant to the test and could be applied directly to the time series data without having any need to apply standard pre-processing noise reduction techniques and phase space reconstruction. It could be widely applied to datasets generated from maps, ordinary and partial differential equations using deterministic dynamical systems [23], [25]. It is conceived in deterministic systems to distinguish chaotic behaviour from regular behaviour. If the system is chaotic, the test results in a value of 1 and 0 if the system is regular. There was also a suggestion for an implementation technique of the 0-1 test by Gottwald *et al.*, which was very useful for the present study [23], [26]. The synthesis of the 0-1 test was carried out by initially calculating the translational variables known as $p_c(n)$ and q_c (n) in the complex domain as given by (1) & (2). Consider an observable ϕ(j), which denotes time-series data from the experimental analysis, where $j = 1, 2, 3 \ldots N$. Here, N denotes the length of the time-series data. However, in the present work, the computation is proceeded by considering a sampling of time series data with sampled interval $t_s = 5$. Therefore, the resultant length of the time series data $N_s = N/t_s$ is applied on the obtained pressure time-series data (ϕ (j)) and finally resulting in a sampled pressure time-series data (ϕ_s (j)). By incorporating sampling into the obtained time series data, it could be possible to curb the effects of oversampling. Randomly sampled values of $c \in [0, 2\pi]$ were chosen for the computation of the translational variables as suggested by [23].

$$p_c(n) = \sum_{j=1}^{n} \phi_s(j) \times \cos(jc) \tag{1}$$

$$q_c(n) = \sum_{j=1}^{n} \phi_s(j) \times \sin(jc) \tag{2}$$

In general, an initial estimate of the dynamics could be judged from the $p_c - q_c$ trajectory, i.e., if the translational variables exhibit a bounded trajectory, then the dynamics of the system could be periodic. On the other hand, if the translational variables exhibit Brownian motion, then the dynamics of the system could be chaotic. To ascertain the dynamics of the system more strongly, the diffusive or non-diffusive behaviour of the translational variables would provide key insights. This would be accomplished by evaluating the time-averaged Mean Squared Displacement (MSD) M_c (n), i.e., the real-time tracking of the $p_c - q_c$ trajectory, giving the researcher an idea about the asymptotic growth rate (K_c). For regular (periodic) dynamics, the mean squared displacement is witnessed to be a bounded function in time, whereas, if the dynamics of the system are chaotic, then the mean squared displacement scales linearly with time.

Computation of the time-averaged mean squared displacement is calculated from the translational variables as given by (3). The limit described in the equation is assured by evaluating M_c (n) only for $n \leq n_{cut}$ where, $n_{cut} \leq N_s$, and in practice, it was assumed that $n_{cut} = N_s/10$ yielded promising results. In addition to computing the mean squared displacement, modification to the algorithm was made by computing the modified mean squared displacement (D_c (n)). This parameter exhibits the same asymptotic growth rate as M_c (n) but with enhanced convergence properties. The oscillatory term V_{osc}(c, n) in (5) regularizes the linear behaviour of M_c (n) and is subtracted from the mean squared displacement yielding the modified mean squared displacement as given by (4).

$$M_c(n) = \lim_{N_s \to \infty} \frac{1}{(N_s - n)} \sum_{m=1}^{N_s - n} \Big[\Big((p_c(m+n) - p_c(m))^2 + (q_c(m+n) - q_c(m))^2 \Big) \Big] \quad (3)$$

where n is quantified as the time index, and $(N_s - n)$ denotes the number of interval samples and,

$$D_c(n) = M_c(n) - V_{osc}(c, n) \quad (4)$$

Here,

$$V_{osc}(c, n) = \left(E_{\phi_s}\right)^2 \times \frac{(1 - \cos(c \times n))}{(1 - \cos c)} \quad (5)$$

The expectation E of the random variable X, in this case; the observable $\phi_s(j)$ is given as

$$E_{\phi_s} = \lim_{N_s \to \infty} \frac{1}{N_s} \sum_{j=1}^{N_s} \phi_s(j) \quad (6)$$

The test for chaos is based on the evaluation of the asymptotic growth rate (K_c) of the modified mean squared displacement (D_c (n)). The value of the asymptotic growth rate (K_c) is measured with the vectors of time ξ and modified mean square displacement Δ. It can be defined as,

$$\xi = (1, 2, 3, \ldots\ldots, n_{cut})^\top \quad (7a)$$

$$\Delta = (D_c(1), D_c(2), D_c(3), \ldots\ldots\ldots\ldots, D_c(n_{cut}))^\top \quad (7b)$$

Now, the value of asymptotic growth rate K_c can be measured with the definition of correlation co-efficient. It is defined as,

$$K_c = corr(\xi, \Delta) = \frac{cov(\xi, \Delta)}{\sqrt{var(\xi) \times var(\Delta)}} \in [-1, 1] \quad (8)$$

Here,

$$cov(\xi, \Delta) = \frac{1}{n} \sum_{j=1}^{n} \left((\xi(j) - \bar{\xi}) \times (\Delta(j) - \bar{\Delta}) \right) \quad (9)$$

And

$$var(\xi) = cov(\xi, \xi) \quad (10)$$

Here,

$$\bar{\xi} = \frac{1}{n} \sum_{j=1}^{n} \xi(j) \quad (11)$$

$$\bar{\Delta} = \frac{1}{n} \sum_{j=1}^{n} \Delta(j) \quad (12)$$

$$K = median(K_c) \quad (13)$$

The test was conducted for $N_c = 100$ values of c, and the final K value was determined by computing the median of these K_c values as shown in (13). An ideal value of $K \approx 0$, indicates periodic dynamics; and a value of $K \approx 1$, indicates chaotic dynamics. Also, a value in between the mentioned range $K \in [0,1]$, could either denote the transition of the dynamics from periodic to chaotic or vice–versa.

III. MATERIALS AND METHODS

In any experimental routine, dealing with wind tunnel experiments involves either force measurement or the pressure measurement technique. The latter is utilized to understand the pressure distribution or rather the flow-field around the airfoil at each point on the surface and appropriately make judgments on the aerodynamic characteristics of the airfoil under consideration. Since the pressure that is to be measured on the surface; requires a high level of accuracy, sophisticated experimental procedures would have to be followed to avoid any experimental errors.

A. SIMULTANEOUS PRESSURE SCANNER

To understand the underlying dynamics of the surface pressure characteristics over ice accreted airfoils, simultaneous surface pressure measurements were carried out. The synthesis of the experimental work involves the acquisition of the instantaneous pressure from the pressure taps (ports) located on the surface of the airfoil. This is achieved by incorporating

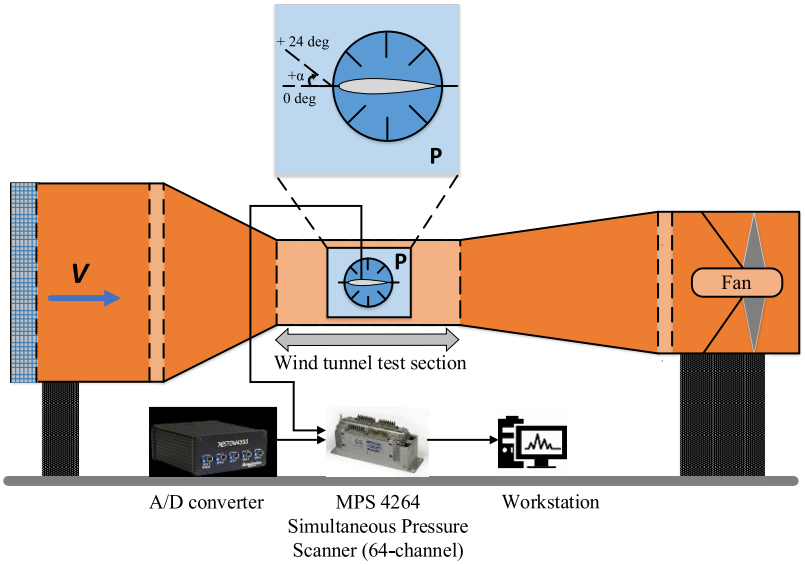

FIGURE 1. Schematic of the low-speed subsonic wind tunnel that was used for the experimental study.

a highly sensitive instrument known as the SCANIVALVE (MPS4264) multi-channel pressure scanner. The pressure ports on the model surface were connected to the pressure scanner with a flexible low–pressure loss tubing, specifically designed to minimize the pressure losses occurring due to various factors like frictional losses, losses due to bends in the pipes, etc. The pressure scanner was pre-programmed to acquire 10000 samples of pressure data from a single channel with a scanning/sampling frequency of 700 Hz. The final value of the pressure at a port could be evaluated as the average of 10000 samples of pressure that were collected. Since the pressure scanner involves the acquisition of instantaneous values of pressure data, it allows the researcher to explore and work on time series data. Hence, this time series data was used as a pre-requisite to be applied to the 0-1 test for chaos to detect the underlying dynamics at each of the pressure ports on the airfoil.

B. WIND TUNNEL AND TEST AIRFOIL

Experimental flow simulations were performed on the low-speed subsonic suction-type wind tunnel situated at the Aerospace Laboratory at SASTRA Deemed University, as shown in Fig. 1. The wind tunnel's test section measures 1500 mm in length and 300 mm × 300 mm in cross-section. The tunnel is powered by a 10 HP motor, and the maximum velocity inside the test section of the wind tunnel could reach up to 60 m/s. The freestream turbulence intensity inside the test section was less than 0.51%. The experiment was conducted at a Reynolds number of 2.03×10^5 with a freestream velocity of 30 m/s. To achieve a steady and uniform flow in the test section, flow straighteners made from honeycomb structured grids were installed at the entry of the effuser. The angle of attack of the airfoil was varied from 0° to 24° with an increment of 3° each.

A 3D printed rectangular symmetrical airfoil using PLA material with the surface roughness of 100 micros is used for the current experimental work. The airfoil was designed to have a maximum thickness of 12% of the chord. A total of 20 pressure ports were located on the surface of the airfoil to measure the instantaneous pressures in the flowfield around the airfoil. The airfoil had a span length of 300 mm and a chord of 100 mm, as shown in Fig. 2. The diameter of the pressure ports was designed approximately 1 mm. The airfoil was horizontally mounted in the wind tunnel with the aid of a cylindrical holder. In addition to this, the arrangement of the airfoil; aided in adjusting the pitch position, and the pitch of the airfoil was measured using the pitch protractor available in the wind tunnel sidewall, as shown in Fig 1.

C. ICE ACCRETED AIRFOIL

The predominant aim of the current experiment was to study the underlying dynamics of the surface pressure characteristics of distinct ice accreted airfoils at each of the pressure ports. The geometry of the ice templates is adapted from NASA's IRT (Icing Research Tunnel), wherein Ching *et al.* Tsao and Anderson [16] have conducted a series of tests to determine the types of formation of ice on the surface of the NACA 0012 airfoil under various conditions as given in Table 1. This paves an opportunity to acquire the geometries of ice from the literature, which contained the x/c, y/c normalized coordinates. Four different geometries of ice were acquired and geometrically modeled to be approximately equal to the normalized coordinates contained in the reference literature, as shown by a schematic in Fig 3 - Fig.6. This ensured that the geometrical similarity was maintained

TABLE 1. Conditions for various ice accretion geometries on NACA0012 airfoil as adapted from the IRT test data at NASA GLENN research centre [16].

Shape of ice	IRT Run no.	Chord (cm)	T_{st} (C^o)	Velocity (m/s)	MVD (μm)	LWC (g/m^3)	Spray Time (τ) (min)
Rime ice type – 1	3-2-02/6	91.4	-23	77	70	0.6	19.3
Rime ice type – 2	9-3-03/5	53.3	-14	77	20	0.5	16.9
Rime ice type – 3	8-9-03/3	91.4	-21	77	15	0.5	40.8
Horn ice	10-10-02/1	91.4	-8	77	20	1.15	17

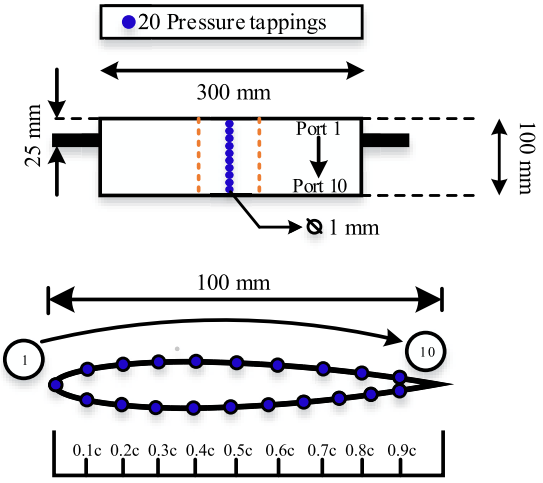

FIGURE 2. NACA 0012 – position of pressure taps (ports) and schematic of the airfoil's geometry.

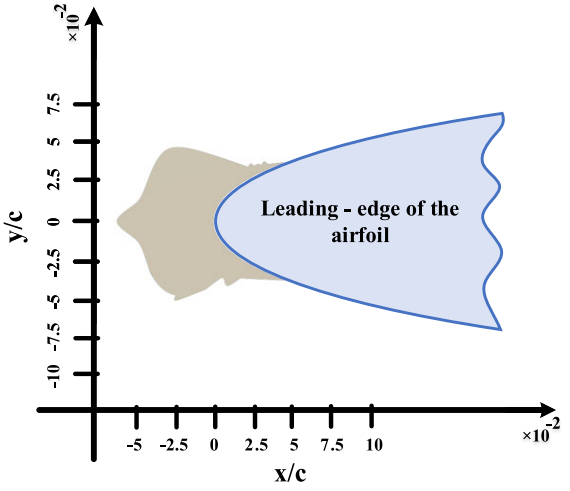

FIGURE 4. Rime ice type 2 accreted airfoil in its normalized coordinate system.

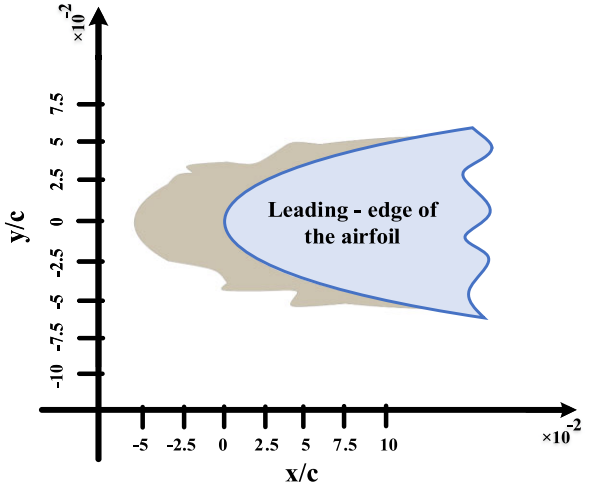

FIGURE 3. Rime ice type 1 accreted airfoil in its normalized coordinate system (c – chord of the airfoil).

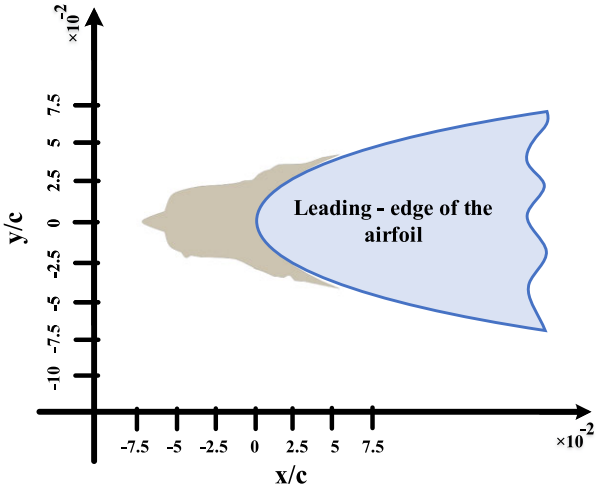

FIGURE 5. Rime ice type 3 accreted airfoil in its normalized coordinate system.

between the 3D printed prototype (ice template) and the actual ice accreted geometry from the IRT. The ice templates were affixed to the leading edge of the airfoil, and the underlying dynamics of the surface pressure characteristics were estimated using the 0-1 test approach.

IV. RESULTS AND DISCUSSIONS

The simultaneous surface pressure measurements were carried out, and the 0-1 test for chaos was utilized to characterize the acquired surface pressures as periodic, chaotic, or transitory; and the results were put forth in detail in this section. This involves estimating the underlying dynamics

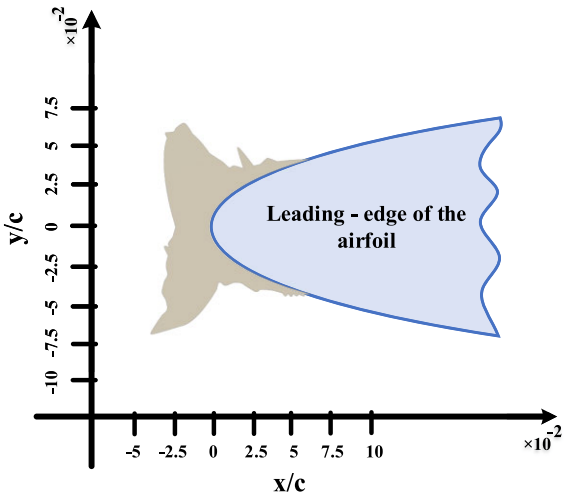

FIGURE 6. Horn ice-accreted airfoil in its normalized coordinate system.

at each pressure port of the airfoil. Doing so would aid in understanding the flowfield around the airfoil and estimate its aerodynamic performance. Though the experiment was conducted for all the angles of attack mentioned in the range, the discussion of results predominantly focuses on the pre–stall and stall angles of attack of the airfoil under consideration. Also, this study does not account for the aerodynamic forces emerging from the shear stress distribution and mainly focuses on the forces occurring purely due to pressure distribution around the airfoil. In our present study, we first consider the discussion of the quantitative and qualitative aspects of the aerodynamic coefficients, followed by the surface pressure dynamics of the baseline and ice-accreted airfoil using the 0-1 test. However, estimating the coefficient of pressure (C_p) plot to study the flow field around the airfoil would only serve as a preliminary tool since the pressure at each port is the average of all the pressures over a time interval. This might not put forth firm insights about the flow field, due to the loss of information on the dynamics of the system. To judge the dynamics of the system with ease, the 0-1 test for chaos has been implemented, which elucidates the dynamics of the system with a single value $K = 0$ (Periodic dynamics) or $K = 1$ (Chaotic dynamics). In addition to this, a value of K between 0 and 1 could significantly refer to the transitory dynamics of the system.

A. DISCUSSION OF THE AERODYNAMIC COEFFICIENTS: COEFFICIENT OF LIFT (C_L) & COEFFICIENT OF DRAG (C_D)

The aerodynamic coefficients C_L and C_D were computed for the baseline and the ice-accreted airfoil as shown in Fig. 8 and Fig.9. It could be ascertained that for the baseline airfoil, the coefficient of lift (C_L) increases with an increase in the angle of attack of the airfoil up to $\alpha_{stall} = 12°$ with a maximum C_L of 0.59.

The C_L was compromised when the angle of attack of the airfoil was further increased after the stall angle of attack (α_{stall}). The lift curve slope ($dC_L/d\alpha$) was acknowledged to be approximately equal to 0.075 deg^{-1} for $0° \leq \alpha \leq 6°$. After the stall angle of attack, the lift curve slope experienced a rapid decrease in its value with -0.0394 deg^{-1} for $12° \leq \alpha \leq 15°$. This implied the onset of flow separation and its associated negative effects which, decreased the aerodynamic performance of the airfoil after α_{stall} as is evident from the pressure distribution plot shown in Fig 10. Considering the rime ice type 1 airfoil, the lift curve slope was seen to be approximately equal to the baseline up to $\alpha = 6°$. The lift curve slope for $6° \leq \alpha \leq 12°$ was witnessed to be approximately equal to 0.045 deg^{-1} when compared to the lesser slope witnessed for the baseline airfoil. The rime ice type 1 airfoil also stalls at $\alpha = 12^{\circ}$ but with a maximum C_L of 0.68. This increment in C_{Lmax} could be due to the introduction of local turbulence generated due to the distortions in the geometry of the rime ice formed. Generally, the turbulent flow could overcome the adverse pressure gradient much efficiently than the laminar flow, and hence, the flow remains attached for a longer time. However, the rime ice type 1 and 3 geometry approximately resemble the leading edge of the test airfoil, but the flow over the rime ice type 3 accreted airfoil could approximately resemble that of the baseline case; in addition to the fact that the rime ice type 1 and 3 produce less distortion to the flow – field when compared to the rime ice type 2 and horn ice accreted airfoil. From Fig 7, it could be acknowledged that the amplitude of % change in C_L fluctuations was minimum for the rime ice type 1 and rime ice type 3 when compared to the horn ice and rime ice type 2 airfoil. For the rime ice type 2 geometry, the lift curve slope almost resembles that of the baseline until $\alpha = 6°$. Thereafter, the slope of the lift curve decreases to a significant amount with a $\alpha_{stall} = 9^{\circ}$ and a $C_{L,max}$ of 0.44, as evident from Fig. 8 and Fig.12.

Observing the horn iced airfoil, it experiences an early stall at $\alpha_{stall} = 3°$ with a significant reduction in the maximum coefficient of lift ($C_{L,max}$) to 0.32. This loss in the aerodynamic performance of the horn ice-accreted airfoil could be due to a geometry resembling the flow separation bubble, usually a recirculating region caused by the horn ice geometry. The bubble seems to dominate the flowfield and hence affects the pressure distribution around the airfoil, aiding the rise in pressure drag evident from Fig. 9. Initially, the recirculation region seems to occur in the immediate downstream region, and the flow tries to reattach to the surface by entraining fluid molecules from the free - stream, contributing to a successful pressure recovery evident from Fig. 14. For the range $3° \leq \alpha \leq 6°$, due to the strong adverse pressure gradient, the flow begins to separate due to the breakdown of the recirculating region and never attempts to reattach to the surface. Hence, an iso- pressure is witnessed from $\alpha = 6°$ at all x/c locations on the airfoil. This could indicate evidence of a complete flow breakdown and its adverse aerodynamic effects. Thus, the horn ice-accreted airfoil was witnessed to perform significantly weaker when compared to all the other ice accreted airfoils, as shown from Fig. 7, Fig. 8, Fig. 9, and Fig. 14. The dynamics of the surface pressure

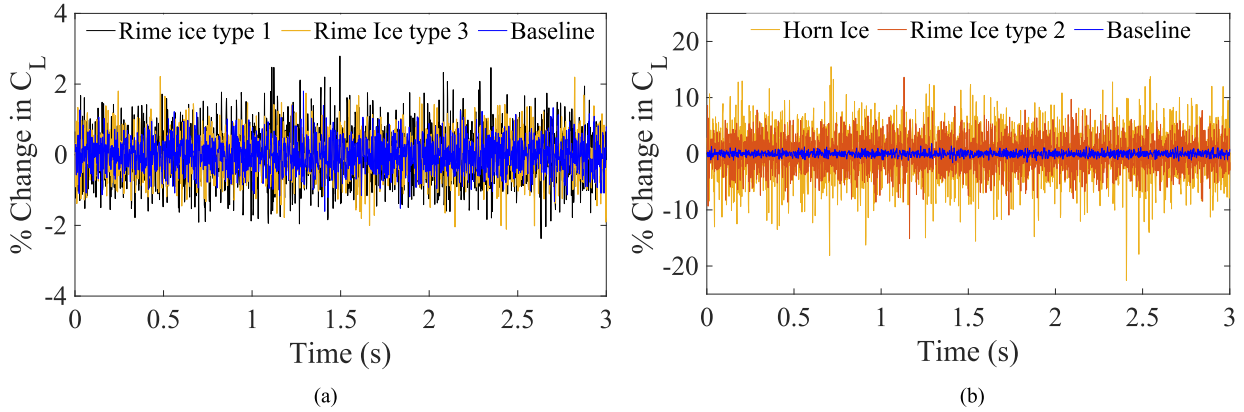

FIGURE 7. (a). Percentage change in C_L vs time (s) for baseline, rime ice 1 and rime ice 2 airfoils at an angle of attack (α) = 3°. (b). Percentage change in C_L vs time (s) for baseline, rime ice 2 and horn Iced airfoils at an angle of attack (α) = 3°.

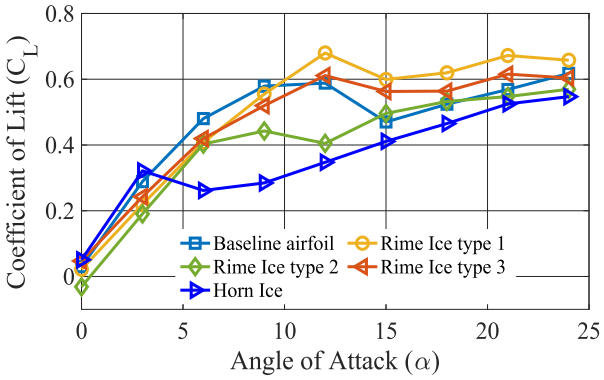

FIGURE 8. Coefficient of lift (C_L) vs angle of attack (α) for baseline and ice accreted airfoils at Re = 2.0 × 105.

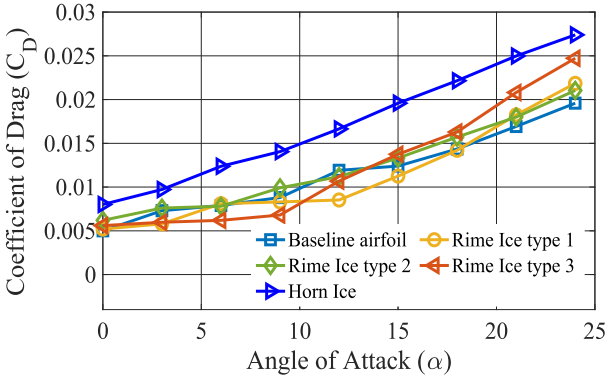

FIGURE 9. Coefficient of drag (C_D) vs angle of attack (α) for baseline and ice accreted airfoils at Re = 2.0 × 105.

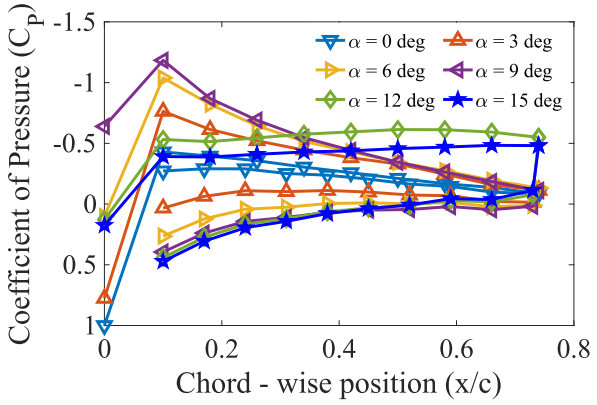

FIGURE 10. Coefficient of pressure (CP) vs chordwise position (x/c) for baseline airfoil.

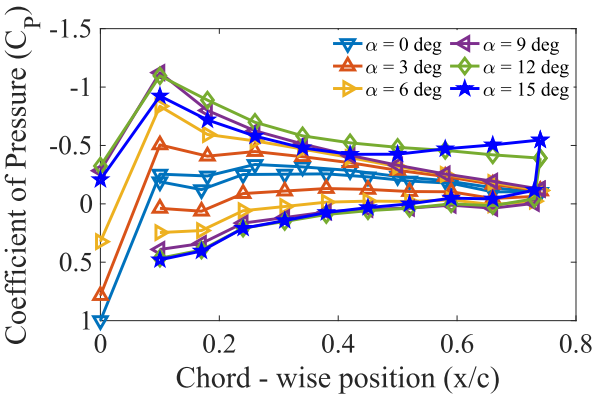

FIGURE 11. Coefficient of pressure (CP) vs chordwise position (x/c) for rime ice-type 1 airfoil.

characteristics and their associated effects would be discussed in the subsequent sub-section IV.B.

B. DYNAMICS OF THE PRESSURE PORTS ON THE SUCTION SURFACE OF THE BASELINE AND ICE ACCRETED AIRFOILS

1) SURFACE PRESSURE DYNAMICS OF BASELINE AIRFOIL

Initially, the flow inside the test section is steady and uniform; hence, the first pressure port, i.e., the stagnation point (port 1) at $\alpha = 0°$, experiences periodic inflow giving a value of K ≈ 0 as shown in Fig. 15. In the case of the asymmetrical airfoil at 0° angle of attack, the flow accelerates on the suction surface and pressure surface with approximately equal magnitude, and hence, there is no significant pressure difference witnessed, as evident from Fig 10. Due to this, the coefficient of lift (C_L) acting on the airfoil was

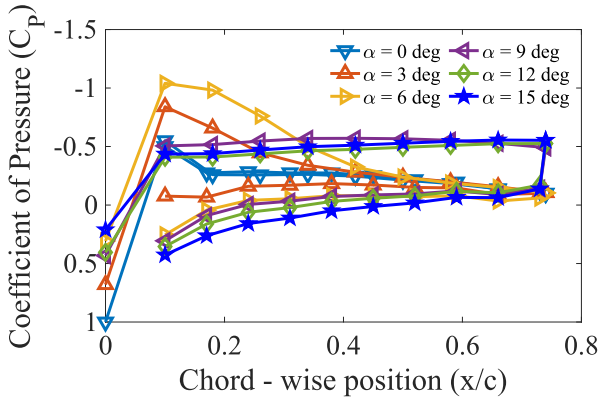

FIGURE 12. Coefficient of pressure (CP) vs chordwise position (x/c) for rime ice type 2 airfoil.

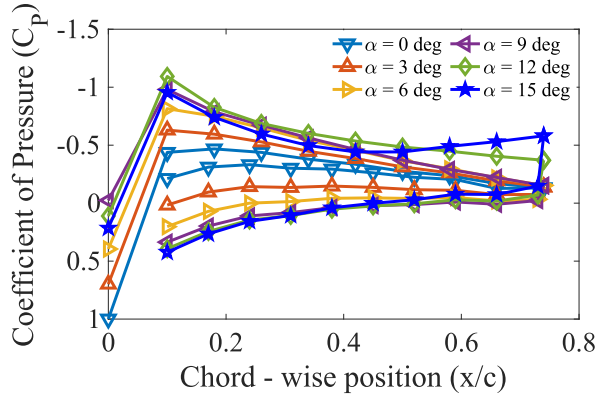

FIGURE 13. Coefficient of pressure (CP) vs chordwise position (x/c) for rime ice type 3 airfoil.

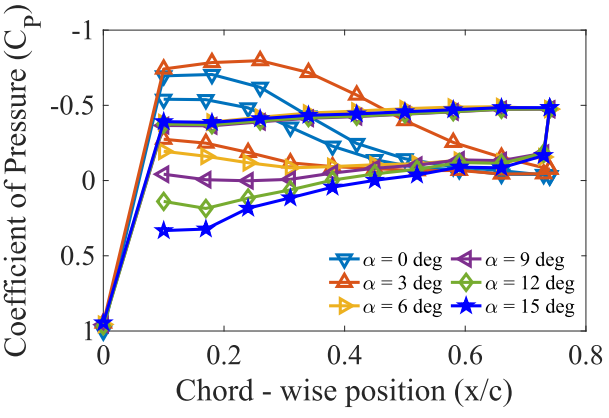

FIGURE 14. Coefficient of pressure (CP) vs chordwise position (x/c) for horn iced airfoil.

approximately equal to zero. At $\alpha = 0°$, the flow bifurcates equally at the stagnation point, and the acceleration of the flow from the leading edge could cause the laminar flow to be still periodic on the suction surface of the airfoil. As the flow traverses downstream, the cross-sectional area of the so-called stream - tube increases and hence, the increase in static pressure. In general, in a strong unfavourable pressure gradient, the pressure force could dominate the fluid's inertial force, and hence, the boundary layer tends to separate from the surface of the airfoil. However, at lower adverse pressure gradients, the flow begins experiencing pressure recovery. The laminar boundary layer becomes unstable to minor perturbations, due to which the transition occurs inside the boundary layer and could grow into a turbulent boundary layer through the primary and secondary mode of instabilities in the transition process. In the case of the baseline airfoil at $\alpha = 0°$, the rise in pressure along the flow direction on the rear half of the airfoil was created due to a less significant adverse pressure gradient, thereby leading to flow separation close to the trailing edge. This shows weakly chaotic behaviour at pressure port 10, as evident from the value of $K \rightarrow 1$ in Fig. 15.

As the angle of attack of the airfoil increases to $\alpha = 6°$, it could bring about a gradual increase in the adverse pressure gradient downstream of the airfoil. The laminar boundary layer from the leading-edge experiences' acceleration at pressure ports 2, 3, and 4 i.e., approximately at the locations $0 < x/c \leq 0.3$ as evident from Fig. 16, and hence the value of $K \approx 0$. Thereafter, the laminar boundary layer experiences a weak transition to turbulence under the increasing pressure gradient at pressure ports 6 – 9, as evident from Fig. 16. It could be possible that a complete turbulent boundary layer was not developed, and there could be a possibility for the existence of a laminar sub-layer within the turbulent boundary layer. This paves the way for the flow to be weakly chaotic at the downstream pressure ports, as explained by the K values shown in Fig. 16. At a critical value of the momentum thickness Reynolds number (Re_θ), the laminar boundary layer experiences transition to turbulence and completely evolves into a turbulent boundary layer. If this would be the case, then the underlying dynamics would have been chaotic. In general, periodic behaviour of the surface pressure could be observed at the point of stagnation of the flow. As the angle of attack is increased, the front stagnation point gradually shifts on the pressure side and moves farther from the leading edge. Since there is a low pressure created on the upper surface closer to the leading edge due to the acceleration of the flow, the stagnating streamline bifurcates and attempts to flow towards the region of low pressure. When the airfoil is at an angle of attack, the bifurcation of the flow from the stagnation point could be aperiodic but, otherwise, for the airfoil at 0° angle of attack. This bifurcated part of the flow tends to join with the incoming streamline periodically, and this aperiodicity could be unpredictable for a particular angle of attack. Thus, pressure port 1 experiences chaos at $\alpha = 6°$ and significantly higher chaotic surface pressure at $\alpha = 12°$ compared to that of the previous case.

As the angle of attack was increased further to $\alpha = 12°$, the flow experiences an adverse pressure gradient, and the separation point shifts away from the trailing edge closer to the leading edge of the airfoil. At this angle of attack, the flow tries to accelerate but then experiences complete breakdown after pressure port 2 evident from Fig. 16 and hence, the separated shear layer never reattaches onto the surface of the airfoil. This separated shear layer could initially tend to form eddies and vortices downstream of the airfoil due to the

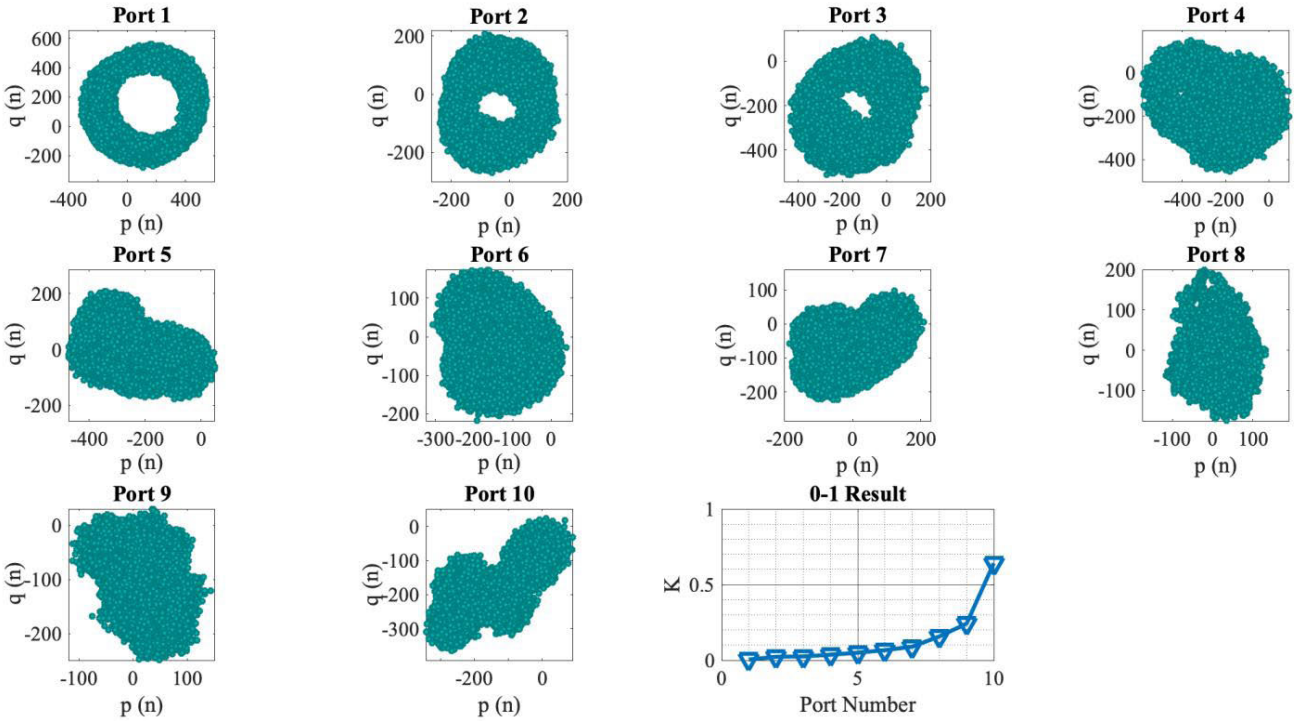

FIGURE 15. 0-1 test results of the pressure data obtained on the suction surface of the baseline airfoil at $\alpha = 0°$.

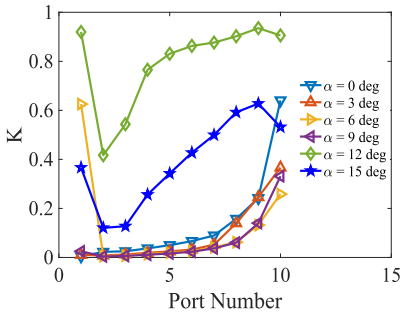

FIGURE 16. 0-1 test results obtained over the suction surface of the baseline airfoil.

adverse pressure gradient after the separation point; through Kelvin – Helmholtz instability (primary mode of instability in transition process) [27]. Thereafter, the higher growth rate of disturbances through the secondary mode of instability propagates and a large region of the turbulent wake is created and henceforth, the value of K $\rightarrow$ 1. This paves way for an unsteady and chaotic flowfield as witnessed from the K values shown in Fig. 16 for $\alpha = 12°$.

2) SURFACE PRESSURE DYNAMICS OF RIME ICE TYPE-1 AIRFOIL

In the case of the rime ice type 1 geometry at $\alpha = 0°$, the flow was witnessed to stagnate at pressure port 1 as usual, and hence, the value of K $\approx$ 0 was acknowledged. The bypass transition process causes the flow to be initially laminar on the surface of the airfoil through the formation of Klebanoff distortions/streaks characterized by long streamwise perturbations as explained by Liu *et al.* [28]. These streaks tend to inhibit the growth rate of Tollmien-Schlichting (TS) waves and delay the transition process. These TS waves are responsible for the amplification of perturbations in the flow, which is known to be the primary instability mode for attached boundary layers. U – component perturbations oscillate periodically in the spanwise elongated direction, as claimed by [28]. In a bypass transition of the boundary layer, either tripping the boundary layer or introducing free stream turbulence could cause the phenomenon downstream by bypassing the initial phases of the natural laminar-turbulent transition. Due to the distortions on the surface of the rime ice type 1 geometry, the flow experiences bypass transition by tripping the boundary layer to turbulence. Pressure ports 2 and 3 experienced weak chaotic behaviour (K = 0.1), as evident from Fig 17. The weak chaotic behaviour could be due to the small-scale perturbations introduced immediately into the flow. The dynamics of the system could significantly depend on the intensity of turbulence due to tripping and the surface pressure gradient at which the bypass transition occurs. Further, when the flow traverses along the suction surface of the airfoil from the leading edge, the flow experiences significant acceleration due to the favourable pressure gradient and dampens the small-scale perturbations. Hence, the weak chaoticity of the surface pressure dropped and remained closely periodic till pressure port 6. After that, when the flow achieves successful pressure recovery, the flow tends to lose its periodic structure, and the inception of transition

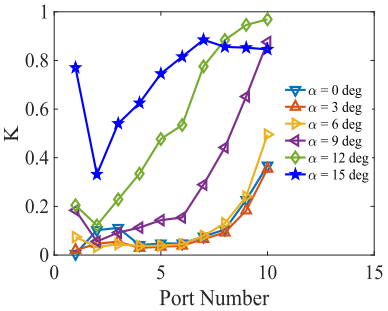

FIGURE 17. 0-1 test results obtained over the suction surface of the rime ice type 1 accreted airfoil.

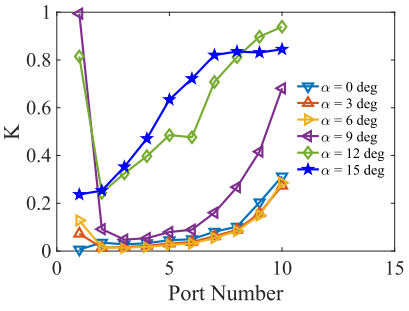

FIGURE 18. 0-1 test results obtained over the suction surface of the rime ice type 3 accreted airfoil.

to turbulence begins. This phenomenon could be witnessed from pressure port 6, apparent from the K values in Fig 17 for $\alpha = 0°$. However, a completely turbulent boundary layer was not developed due to the weak transition process. Also, when the secondary instability is weak (favourable pressure gradient / low adverse pressure gradient), the flow becomes more stable due to the inhibition of the growth rate of primary TS waves and delays the transition process. When the secondary instability mode is significantly strong (strong adverse pressure gradients), the boundary layer streaks promote an early transition to turbulence through primary followed by the secondary mode of instabilities.

This phenomenon was witnessed at $\alpha = 9°$, due to the adverse pressure gradient significantly increasing along the airfoil in the downstream direction. Inception and growth of turbulent spots appear in the early stages of the transition, and hence, a developing turbulent boundary layer was witnessed closer to pressure port 10 as evident from $K \rightarrow 1$ shown in Fig 17 for $\alpha = 9°$. However, the flow seems to behave weakly chaotic when traversing from pressure ports 2 to 6 with the value of $K \rightarrow 0.175$. This could be a transition through the primary mode of instability on the suction surface of the airfoil. After pressure port 6, the flow experiences transition through a secondary mode of instability, and hence, the flow tends to lose its periodic behaviour steeply until a completely turbulent boundary layer was formed. The primary mode of instability may be active until the disturbances grow where nonlinear growth begins. The second mode of instability may be active with the onset of nonlinear growth in disturbances.

Increasing the angle of attack further to $\alpha = 12°$ caused a significant increase in the adverse pressure gradient. From Fig 8, it could be witnessed that the rime ice type 1 airfoil stalls at $\alpha = 12°$ like the baseline case. As explained earlier, pressure port 2 experienced periodic behaviour as the flow was initially laminar due to the formation of Klebanoff distortions/streaks. At an increased adverse pressure gradient, the transition of the boundary layer streaks to turbulence was preponed earlier (compared to that of the case at $\alpha = 9°$) by the formation of turbulent spots on the suction surface of the airfoil. The turbulent spots/zones grow until they coalesce to form a turbulent boundary layer. Hence, the slope of the K curves for $\alpha = 12°$ was seen to be higher than at $\alpha = 9°$ from pressure ports 2 – 6, evident from Fig 17. Thereafter, the growth rate of the disturbances could have significantly increased by a larger amount through the secondary instability mode and finally led to the evolution into a turbulent boundary layer with the value of $K = 1$ at pressure port 10. For the baseline case, the flow was witnessed to completely break down after pressure port 2. However, for the rime ice type 1 airfoil at $\alpha = 12°$, the flow remains attached to the surface of the airfoil without getting separated, rather than in the case of the baseline airfoil at $\alpha = 12°$. This could be evident from the value of K at pressure ports 2 – 6, wherein the chaoticity was significantly less for the attached flow. However, the completely broken-down flow exhibits high chaoticity. Usually, the turbulent boundary layer could overcome the adverse pressure gradient significantly better than the laminar flow and hence, remains attached over the suction surface of the airfoil. This could be the reason behind the slight increase in the maximum coefficient of lift ($C_{L,max}$).

3) SURFACE PRESSURE DYNAMICS OF RIME ICE TYPE 3

In the case of the rime ice type 3 airfoil, the flow characteristics resemble that of the baseline airfoil because this geometry resembles the leading edge of the airfoil approximately. Due to the spearhead-like protrusion on the rime ice type 3 geometry, the effective geometry of the airfoil is aerodynamically enhanced. Hence, at $\alpha = 0°$, $3°$ and $6°$, the disturbance created in the flowfield are minimal and hence the surface pressure characteristics exhibit weak chaos as evident from Fig 18. At $\alpha = 9°$, pressure port 1 experiences chaotic surface pressure behaviour consistent with the previous explanations on flow bifurcation. The flow accelerates at pressure port 2 as usual, and due to the increasing pressure gradient, the laminar boundary layer experiences a transition to turbulence. This produces chaotic surface pressure behaviour closer to the trailing edge, consistent with the previous explanations made for the transition process. At $\alpha = 15°$, due to the presence of the spearhead, it could contribute to an increase in the pressure gradient with an increase in the angle of attack. This phenomenon could energize the perturbations in the flow – field and hence paves way for an earlier transition to turbulence. This is evident with a higher slope of the K curve up to port 5 for $\alpha = 15°$ when compared to lesser angles of attack, as shown in Fig 18.

4) SURFACE PRESSURE DYNAMICS OF RIME ICE TYPE 2 AIRFOIL

It could be acknowledged that for the rime ice type 2, the height of the discontinuity was significantly less than that of the horn iced airfoil. Nevertheless, at $\alpha = 0°$; pressure port 1 (Stagnation pressure port) experienced periodic surface pressure due to the inflow being steady and uniform. Due to the diminutively increasing pressure gradient, the laminar boundary layer could become mildly unstable to small perturbations through the primary instability mode. However, the length scale of this increasing pressure gradient created by the ice geometry is significantly small when compared to the chord of the airfoil. Hence, these small–scale perturbations cause the flow to experience a weak transition to turbulence and hence, the value of $K \approx 0.49$. But it could be ascertained that for weak transition conditions, the flow could undergo relaminarization under favourable pressure gradient and could cause sufficient damping to perturbations. Hence, the surface pressure dynamics show nearly periodic behaviour at pressure port 6 when compared to pressure port 3 as evident from Figs 19 and 20. Thereafter, the flow experiences a mild adverse pressure gradient due to the increasing area of the stream tube, and hence, the laminar boundary layer experiences transition to turbulence again with $K \to 0.6$ as evident from Fig 20. The localized regions of turbulent spots grow until it coalesces to form a completely turbulent boundary layer. But the boundary layer is still under transition and complete development of the turbulent boundary layer was not witnessed. The flow at the rear half of the rime ice type 2 airfoil at $\alpha = 0°$ was like that of the flow over the baseline airfoil at the same angle of attack as evident from the K curves.

From Fig 8, it was acknowledged that the rime ice type 2 airfoil was witnessed to stall at $\alpha = 9°$ as also evident from the pressure distribution plot shown in Fig 12. Also, a fully developed stall was witnessed only at this angle of attack due to the complete breakdown of the boundary layer, created by a strong adverse pressure gradient. Hence, the flow separates closer to the leading edge of the airfoil (i.e., at pressure port 2 approximately), and the separated shear layer never attempts to reattach to the surface causing a significant region of wake downstream of the airfoil. 0-1 test results reveal that, since the flow accelerates on the upper surface of the airfoil, the flow is initially laminar and hence, the value of $K \approx 0.15$. As the flow progresses downstream, the laminar shear layer experiences transition to turbulence through the primary mode of instability, usually through Kelvin – Helmholtz instability. The small-scale perturbations are amplified through this mode of instability and paves way for the inception and growth of transition towards turbulence as witnessed from pressure ports 2 – 4, where the slope of the K curve increases sharply. After pressure port 4, the growth rate of disturbances increases further and the transition towards a fully turbulent wake now happens through the secondary mode of instability. The significant region of wake created downstream of the airfoil causes the flow to be chaotic on the surface, and hence, the value of $K \to 1$ from pressure ports 6-10 as shown in Fig. 20 for $\alpha = 9°$.

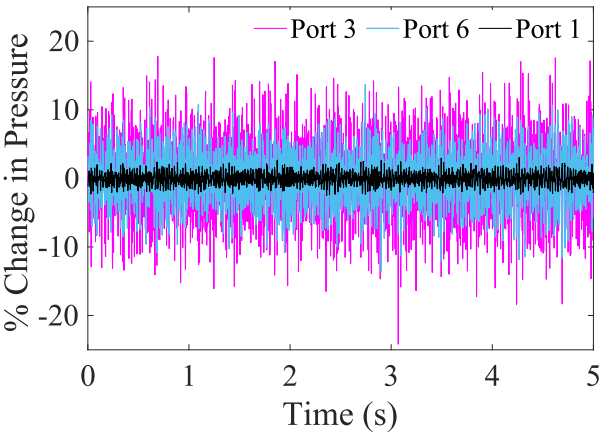

FIGURE 19. Time series of the rime ice type 2 accreted airfoil at pressure ports 1, 3 and 6 at $\alpha = 0°$.

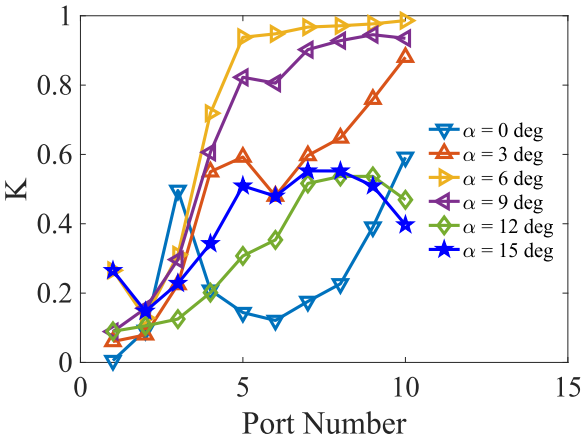

FIGURE 20. 0-1 test results obtained over the suction surface of the rime ice type 2 accreted airfoil.

5) SURFACE PRESSURE DYNAMICS OF HORN ICED AIRFOIL

The horn iced airfoil was witnessed to perform aerodynamically weaker than its counterparts as evident from Figs 8 and 9. At $\alpha = 0°$, pressure port 1 (Stagnation pressure port) experiences periodic surface pressure ($K \approx 0$) due to the steady and uniform inflow into the test section of the wind tunnel as evident from the $P_c - Q_c$ map for port-1 in Fig 21. Due to the strong adverse pressure gradient developed due to the geometry of the horn ice, the boundary layer gets separated from the surface of the horn. This free shear layer developed from the surface of the horn is highly unstable to small–scale perturbations. It traverses downstream and the instability could strongly grow over time. This could initiate the laminar-turbulent transition process and could result in the reattachment as a turbulent boundary layer probably through a geometry resembling a Laminar Separation Bubble (LSB) or otherwise known as the recirculation region.

The region between the separation and the turbulent boundary layer reattachment is the formation of this separation

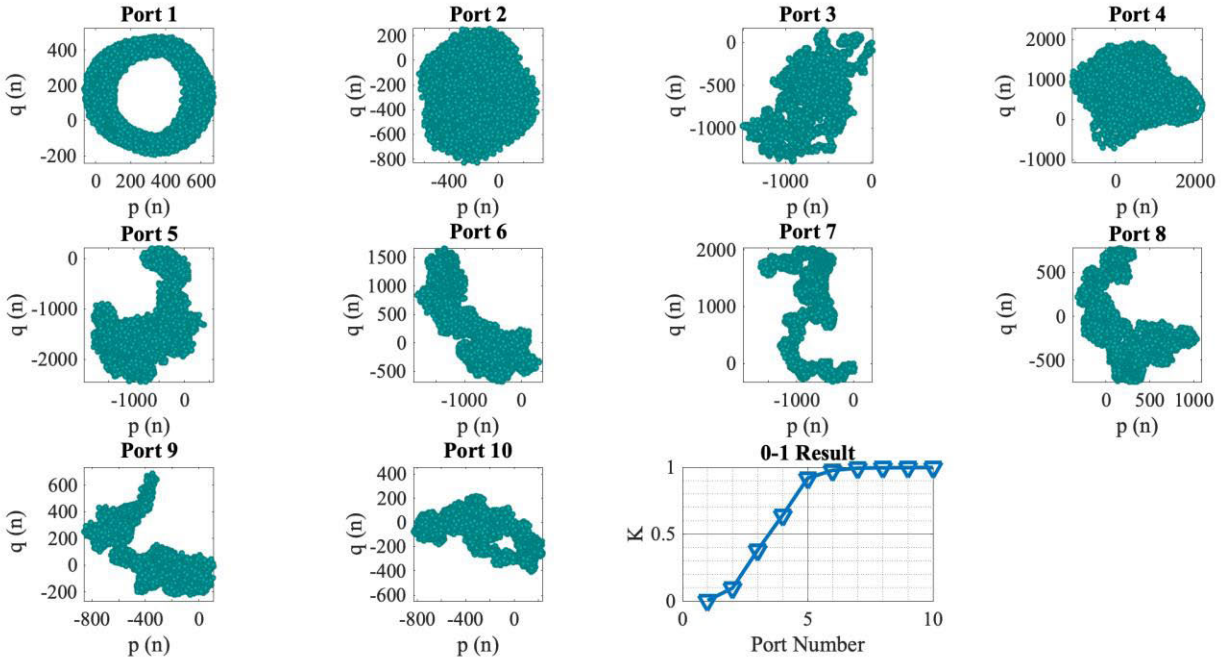

FIGURE 21. 0-1 test results of the pressure data obtained on the suction surface of the horn iced airfoil at $\alpha = 0°$.

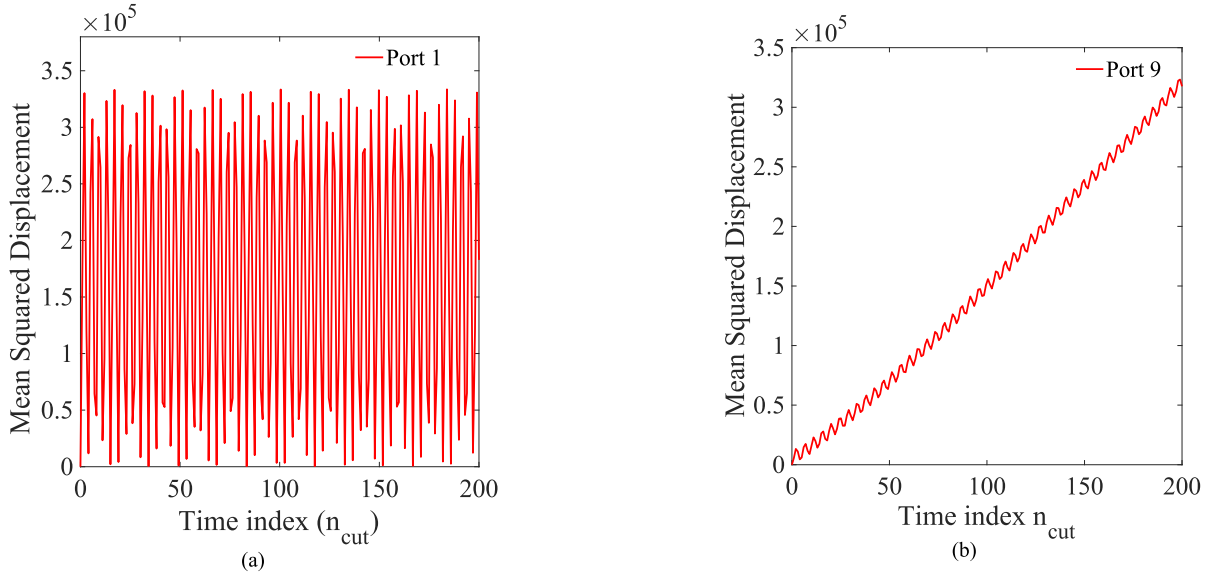

FIGURE 22. (a). Mean squared displacement of the translational variables at pressure port 1 for horn iced airfoil at $\alpha = 0°$. (b). Mean squared displacement of the translational variables at pressure port 9 for horn iced airfoil at $\alpha = 0°$.

bubble, which ranges approximately from $0.1 \leq x/c \leq 0.18$ at $\alpha = 0°$ as shown in Fig 23. However, the mean pressure inside the bubble remains constant as evident from the iso–pressure region in the coefficient of pressure (C_P) plot as shown in Fig 14. Also, the flow experiences a transition from laminar to turbulent flow within the bubble which is a recirculating zone. Henceforth, the flow is laminar (periodic) at the beginning of the bubble at the initial phase of the free shear layer development, and hence, the value of $K = 0.1$. Thereafter, instabilities could grow in the resulting free shear layer, and transition to completely turbulent boundary layer occurs in the downstream of the airfoil coherent with a sharp increase in the K value as shown in Fig 25 for $\alpha = 0°$. When the formation of a turbulent boundary layer aft of the bubble becomes possible, the flow gradually tends to evolve into a chaotic flow – field with the value of $K \rightarrow 1$. Due to the increasing perturbations downstream of the airfoil, the flow experiences transition to turbulence, and depending on the strength of perturbations and growth rate, the transition to completely turbulent boundary layer or in the transition

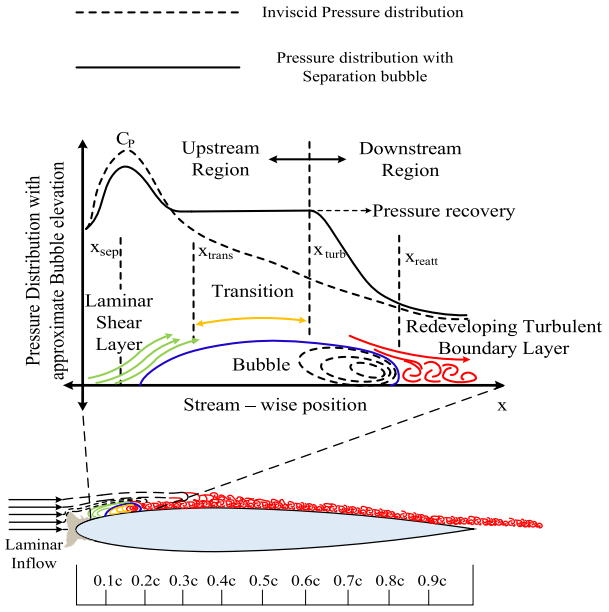

FIGURE 23. Schematic of the flow characteristics of a leading-edge separation bubble on the surface due to horn ice at $\alpha = 0°$.

to turbulent boundary layer is of central focus during the transition process. From the 0-1 test results, it could be correlated that as the K value approaches close to 1, the point where the curve plateaus completely thereafter could be acknowledged to be a completely developed turbulent boundary layer as observed from pressure ports 7 – 10 in Fig 25 for $\alpha = 0°$ and $\alpha = 3°$. On the other hand, when the K value increases until the growth rate of perturbations in the flow reach steady-state chaos i.e., K = 1, the flow could experience the transition to turbulence, or in other words, it is a developing turbulent boundary layer. For strong chaotic dynamics as observed at pressure port 9 for $\alpha = 0°$, the mean squared displacement scales linearly with time as evident from Fig 22(b). For regular dynamics as observed at pressure port 1, the mean squared displacement was witnessed to be a bounded function in time, as evident from Fig 22(a). The amplitude of the % change in pressure, as shown in Fig 24, correlates well with that explained by the K values in Fig 25 for $\alpha = 0°$.

Increasing α to 3° substantially increased the adverse pressure gradient downstream of the airfoil. However, the flow was witnessed to stagnate at pressure port 1 like the case at $\alpha = 0°$ consistent with the previous explanations on flow bifurcation. Nevertheless, no significant changes to the flowfield were witnessed when the angle of attack was increased from $\alpha = 0°$ to $\alpha = 3°$ as evident from the K curve shown in Fig 25. But it could be acknowledged that the LSB resembling geometry was shifted downstream i.e., at $0.18 \leq x/c \leq 0.26$, with an increase in the angle of attack of the airfoil as shown by C_P plot in Fig 14. The horn ice-accreted airfoil was witnessed to stall at this angle of attack, and with a maximum C_L of 0.32, as evident from Fig. 8 and Fig. 14. The formation of a separation bubble could affect the flowfield significantly and cause a decrement in the aerodynamic

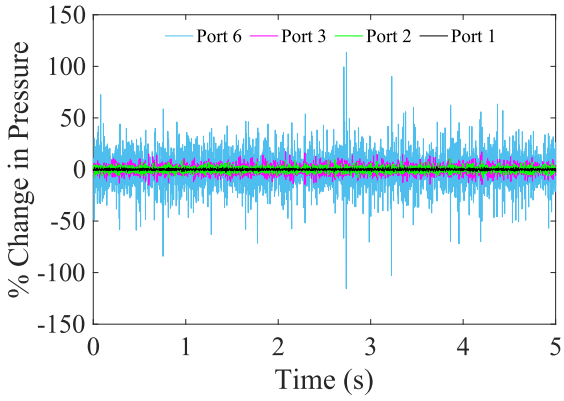

FIGURE 24. Time series of the horn ice-accreted airfoil at pressure ports 1, 2, 3 and 6 at $\alpha = 0°$.

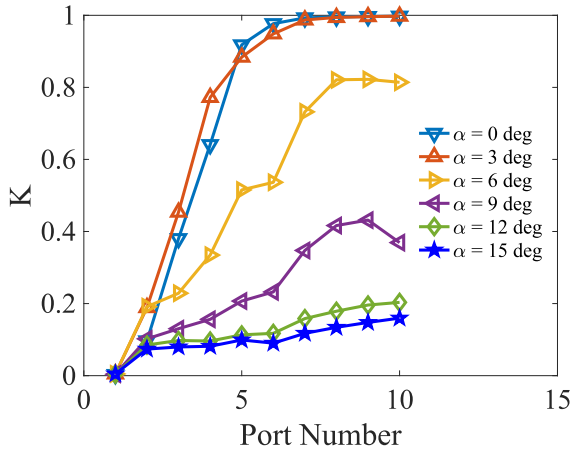

FIGURE 25. 0-1 test results obtained over the suction surface of the horn ice accreted airfoil.

performance with a drastic loss in lift and a significant increment in the pressure drag.

Due to the presence of the horn geometry, a gradual increase in the angle of attack of the airfoil after stall could inhibit the flow to certainly attach to the surface of the airfoil. It could be that the pressure ports might have experienced the flow very weakly, or a region of the dead zone could have been created. Hence, the intensity of chaos in this region could decrease with increasing angle of attack and is coherent with the values of K shown in Fig 25. At $\alpha = 15°$, weak chaotic behavior at the suction surface pressure ports was witnessed when compared to that of the lesser angles of attack. Evidently, as the angle of attack was increased gradually from 0° to 15°; the pressure port 1 was witnessed to certainly experience periodic surface pressure behavior consistent with the explanations provided previously on flow bifurcation. Due to the typical geometry of the horn, it aids the flow to stagnate at pressure port 1 for all the angles of attack by inhibiting the bifurcated flow to traverse to the low-pressure region. Simply, due to the significantly large frontal area of the horn when compared to that of the airfoil, the flow stagnates at pressure port 1 at all angles of attack, and hence, the value of $K \approx 0$ for all the angles of attack of the horn ice accreted airfoil.

V. CONCLUSION

In our present study, the surface pressure characteristics of the baseline and ice accreted airfoils have been carried out using the tools of the 0-1 chaos test to analyze the underlying dynamical transition from periodic to chaotic or vice–versa. The underlying surface pressure dynamics exist in two possible states, i.e., either the periodic state ($K = 0$) or in the chaotic state ($K = 1$). Initially, the freestream flow is steady and uniform, and hence, the stagnation pressure port always experiences periodic surface pressure behaviour at 0° angle of attack. At a positive angle of attack of the airfoil, the flow stagnates at a point on the pressure surface and consequently experiences bifurcation. The bifurcated flow exhibits aperiodicity depending upon the strength of bifurcation and the tendency of the bifurcated part of the flow to traverse to the low-pressure region on the suction surface of the airfoil. Depending on the number of perturbations produced in the flow, the pressure ports close to the leading edge experience periodic / weakly chaotic surface pressure characteristics. As the flow progresses downstream of the airfoil, the magnitude of the adverse pressure gradient could increase, and the small-scale perturbations are amplified through the primary and secondary modes of instabilities. This causes the boundary layer to experience transition towards turbulence. At higher angles of attack, the magnitude of the adverse pressure gradient could significantly increase to a greater amount. At the stalling angle of attack (α_{stall}), the separated flow never reattaches to the surface of the airfoil. This causes the flow – field downstream of the airfoil to be completely chaotic.

The pressure ports on the suction surface of the airfoil, where the value of $K \rightarrow 1$ and remains close to 1 for significantly larger chordwise distance, represents the chaotic flowfield. Besides, when the value of K undergoes the transition to 1, it could denote the transition of the flow from laminar to a turbulent boundary layer. It could be ascertained that the growth rate of perturbations in the flowfield was affected by various factors such as geometry, ice accretion, flow separation, and pressure gradient. For the ice accreted airfoils, the perturbations in the pressure field on the suction surface were predominantly caused by the leading-edge ice geometries. The horn iced airfoil was witnessed to be performing aerodynamically weaker due to the formation of a structure, like a separation bubble, and consequently leading to the creation of a large turbulent wake downstream. Due to this detrimental effect, the maximum coefficient of the lift was witnessed to be minimum for the horn iced airfoil when compared to other ice accretion geometries. The drag on the horn iced airfoil was witnessed to be significantly higher when compared to other ice-accreted airfoil considered in the present study.

This novel and computationally robust test for chaos effectively distinguish between periodic and chaotic dynamics, in addition to the transitory dynamics. Thus, analysis of the underlying dynamics of a deterministic dynamical system could be performed with minimal computational effort. Besides, the test is less susceptible to noise, working directly on the time series data and requiring no phase space reconstruction. Hence, the 0-1 test for chaos greatly outperforms other classical diagnostic tools to detect chaos and can be widely applied to many applications of interest involving the interpretation of the dynamics of a system. The 0-1 test for chaos could be applied to understand the underlying dynamics of the surface pressure characteristics of geometrically modified airfoils.

ACKNOWLEDGMENT

This work was technically and financially supported by the Deanship of Scientific Research (DSR), King Abdulaziz University, Jeddah, under Grant DF-758-135-1441. The authors are thankful to SASTRA Deemed University for allowing us to use the sophisticated wind tunnel testing facility in Turbulence & Flow Control Lab, School of Mechanical Engineering.

REFERENCES

[1] O. Parent and A. Ilinca, "Anti-icing and de-icing techniques for wind turbines: Critical review," *Cold Regions Sci. Technol.*, vol. 65, no. 1, pp. 88–96, Jan. 2011.
[2] O. Yirtici, I. H. Tuncer, and S. Ozgen, "Ice accretion prediction on wind turbines and consequent power losses," *J. Phys., Conf. Ser.*, vol. 753, Sep. 2016, Art. no. 022022.
[3] J. Y. Jin and M. S. Virk, "Study of ice accretion along symmetric and asymmetric airfoils," *J. Wind Eng. Ind. Aerodynamics*, vol. 179, pp. 240–249, Aug. 2018.
[4] A. Hudecz, "Icing problems of wind turbine blades in cold climates," Ph.D. dissertation, Dept. Wind Energy, Tech. Univ. Denmark, Lyngby, Denmark, 2014.
[5] M. Cai, L. Zhou, H. Lei, and H. Huang, "Wind tunnel test investigation on unsteady aerodynamic coefficients of iced 4-bundle conductors," *Adv. Civil Eng.*, vol. 2019, pp. 1–12, Jun. 2019.
[6] J.-X. Li, J. Sun, Y. Ma, S.-H. Wang, and X. Fu, "Study on the aerodynamic characteristics and galloping instability of conductors covered with sector-shaped ice by a wind tunnel test," *Int. J. Struct. Stability Dyn.*, vol. 20, no. 6, Jun. 2020, Art. no. 2040016.
[7] W. Lou, S. Chen, Z. Wen, L. Wang, and D. Wu, "Effects of ice surface and ice shape on aerodynamic characteristics of crescent-shaped iced conductors," *J. Aerosp. Eng.*, vol. 34, no. 3, May 2021, Art. no. 04021008.
[8] M. B. Bragg, A. P. Broeren, and L. A. Blumenthal, "Iced-airfoil aerodynamics," *Prog. Aerosp. Sci.*, vol. 41, no. 5, pp. 323–362, Jul. 2005.
[9] L. P. Raj, J. W. Lee, and R. S. Myong, "Ice accretion and aerodynamic effects on a multi-element airfoil under SLD icing conditions," *Aerosp. Sci. Technol.*, vol. 85, pp. 320–333, Feb. 2019.
[10] M. C. Homola, M. S. Virk, T. Wallenius, P. J. Nicklasson, and P. A. Sundsbø, "Effect of atmospheric temperature and droplet size variation on ice accretion of wind turbine blades," *J. Wind Eng. Ind. Aerodyn.*, vol. 98, no. 12, pp. 724–729, Dec. 2010.
[11] S. G. Pouryoussefi, M. Mirzaei, M.-M. Nazemi, M. Fouladi, and A. Doostmahmoudi, "Experimental study of ice accretion effects on aerodynamic performance of an NACA 23012 airfoil," *Chin. J. Aeronaut.*, vol. 29, no. 3, pp. 585–595, Jun. 2016.
[12] Y. Han, J. Palacios, and S. Schmitz, "Scaled ice accretion experiments on a rotating wind turbine blade," *J. Wind Eng. Ind. Aerodyn.*, vol. 109, pp. 55–67, Oct. 2012.
[13] F. Lamraoui, G. Fortin, R. Benoit, J. Perron, and C. Masson, "Atmospheric icing impact on wind turbine production," *Cold Regions Sci. Technol.*, vol. 100, pp. 36–49, Apr. 2014.
[14] L. Shu, H. Li, Q. Hu, X. Jiang, G. Qiu, G. McClure, and H. Yang, "Study of ice accretion feature and power characteristics of wind turbines at natural icing environment," *Cold Regions Sci. Technol.*, vol. 147, pp. 45–54, Mar. 2018.
[15] L. Hu, X. Zhu, J. Chen, X. Shen, and Z. Du, "Numerical simulation of rime ice on NREL phase VI blade," *J. Wind Eng. Ind. Aerodyn.*, vol. 178, pp. 57–68, Jul. 2018.
[16] J. C. Tsao and D. N. Anderson, "Additional study of MVD effects on ice shapes," in *Proc. AIAA Pap.*, Aug. 2005, pp. 472–480.

[17] S. Arunvinthan, R. Gopal, V. K. Chandrasekar, and S. N. Pillai, "Estimation of nonlinear surface pressure characteristics of aerofoil: A 0-1 test approach," *AIP Adv.*, vol. 9, no. 5, May 2019, Art. no. 055204.
[18] C. Bose and S. Sarkar, "Investigating chaotic wake dynamics past a flapping airfoil and the role of vortex interactions behind the chaotic transition," *Phys. Fluids*, vol. 30, no. 4, Apr. 2018, Art. no. 047101.
[19] S.-W. Li, S. Wang, J.-P. Wang, and J.-C. Mi, "Effect of turbulence intensity on airfoil flow: Numerical simulations and experimental measurements," *Appl. Math. Mech.*, vol. 32, no. 8, pp. 1029–1038, Aug. 2011.
[20] S. Arunvinthan, R. Gopal, V. K. Chandrasekar, and S. N. Pillai, "Recurrence analysis of surface pressure characteristics over symmetrical aerofoil," *Chaos, Interdiscipl. J. Nonlinear Sci.*, vol. 30, no. 1, Jan. 2020, Art. no. 013116.
[21] A. Hadjighasem, M. Farazmand, D. Blazevski, G. Froyland, and G. Haller, "A critical comparison of Lagrangian methods for coherent structure detection," *Chaos, Interdiscipl. J. Nonlinear Sci.*, vol. 27, no. 5, May 2017, Art. no. 053104.
[22] G. A. Gottwald and I. Melbourne, "A new test for chaos in deterministic systems," *Proc. Roy. Soc. London. Ser. A, Math., Phys. Eng. Sci.*, vol. 460, no. 2042, pp. 603–611, Feb. 2004.
[23] G. A. Gottwald and I. Melbourne, "On the implementation of the 0–1 test for chaos," *SIAM J. Appl. Dyn. Syst.*, vol. 8, no. 1, pp. 129–145, Jan. 2009.
[24] G. A. Gottwald and I. Melbourne, "Testing for chaos in deterministic systems with noise," *Phys. D, Nonlinear Phenomena*, vol. 212, nos. 1–2, pp. 100–110, Dec. 2005.
[25] R. Gopal, A. Venkatesan, and M. Lakshmanan, "Applicability of 0-1 test for strange nonchaotic attractors," *Chaos, Interdiscipl. J. Nonlinear Sci.*, vol. 23, no. 2, Jun. 2013, Art. no. 023123.
[26] I. Falconer, G. A. Gottwald, I. Melbourne, and K. Wormnes, "Application of the 0-1 test for chaos to experimental data," *SIAM J. Appl. Dyn. Syst.*, vol. 6, no. 2, pp. 395–402, Jan. 2007.
[27] Z. Yang, "Secondary instability of separated shear layers," *Chin. J. Aeronaut.*, vol. 32, no. 1, pp. 37–44, Jan. 2019.
[28] Y. Liu, T. A. Zaki, and P. A. Durbin, "Floquet analysis of secondary instability of boundary layers distorted by Klebanoff streaks and Tollmien–Schlichting waves," *Phys. Fluids*, vol. 20, no. 12, Dec. 2008, Art. no. 124102.

S. NADARAJA PILLAI received the Ph.D. degree from Tokyo Polytechnic University, Japan, in 2007. He is currently working as an Associate Professor of aerospace engineering with SASTRA Deemed University, India. His research interests include aerodynamics, wind tunnel testing, computational fluid dynamics, wind engineering, and wind turbine aerodynamics. He has received the Early Career Research Award (Young Scientist Scheme) from the Department of Science and Technology, Government of India, in 2017. He was a recipient of the Best Engineer Award from the Institution of Engineers, India, in 2015.

AAKHASH SUNDARESAN received the B.Tech. degree in aerospace engineering from SASTRA Deemed University, Thanjavur, in 2020. He is currently pursuing the Ph.D. degree with IITB-Monash Research Academy. In addition to the B.Tech. course, he was also involved in carrying out active Research at Turbulence and Flow Control Laboratory, SASTRA Deemed University and cleared GATE 2020. Apart from academia, his life centers on mastering the interiority and realization of the self from various dimensions, in correspondence to sharpening the saw before using it as a perfect tool to carry out the desired work.

R. GOPAL received the Ph.D. degree in physics from Bharathidasan University, in 2017. From 2011 to 2016, he was a Senior Research Fellow with the Centre for Nonlinear Dynamics, Bharathidasan University. He has received a Summer Research Teachers Fellowship from the Indian Academy of Sciences, from 2009 to 2011. His research interests include nonlinear dynamics, nonlinear time series analysis, complex networks, and spin-torque nano oscillators.

S. B. M. PRIYA received the Ph.D. degree in wireless communications from Anna University, in 2018. Her research interests include mathematical modeling, machine learning, artificial intelligence, wireless communication, MIMO systems, and wireless networks.

AMJAD ALI PASHA received the Ph.D. degree from the Department of Aerospace Engineering, Indian Institute of Technology Bombay, India. He is currently an Associate Professor and a Researcher with the Aerospace Engineering Department, King Abdulaziz University, Jeddah, Saudi Arabia. His research interests include computational, such as shock/boundary-layer interaction flows, aerofoil wing design, and combustion and convective heat transfer.

ABDUL ZUBAR HAMEED received the Ph.D. degree from the National Institute of Technology, Tiruchirappalli, Tamil Nadu, India. He is currently working as an Associate Professor with the Department of Industrial Engineering, King Abdulaziz University, Saudi Arabia. His research interests include broad areas of flow over cylinders, production engineering and management, robotics and automation, and flow over airfoils.

ABDUL GANI ABDUL JAMEEL received the Ph.D. degree in chemical engineering from the Clean Combustion Research Centre, King Abdullah University of Science and Technology, Saudi Arabia. He is currently an Assistant Professor in chemical engineering with the King Fahd University of Petroleum & Minerals (KFUPM), Saudi Arabia, where he is also a Researcher with the Center for Refining and Advanced Chemicals. His research interests include fuel characterization, pyrolysis and combustion, aerodynamic flows, and machine language applications in combustion.

V. MAHENDRA REDDY received the Ph.D. degree from the Department of Aerospace Engineering, Indian Institute of Technology Bombay, India. He is currently an Assistant Professor with the Department of Mechanical Engineering, IIT Kharagpur. His research interests include flameless/MILD combustion, numerical modeling, low emission combustion, and aerodynamic flows.

KHALID A. JUHANY received the Ph.D. degree in aeronautics and electrical engineering from California Institute of Technology, USA. He is currently the Chairman of the Aerospace Engineering Department, King Abdulaziz University. His research interests include high angles of attack aerodynamics, shock-turbulence interaction, airfoil flows, hypersonic flows, experimental combustion, and propulsion.